SAR Altimeter Backscattered Waveform Model

Chris Ray, Cristina Martin-Puig, Maria Paola Clarizia, *Member, IEEE*, Giulio Ruffini, Salvatore Dinardo, Christine Gommenginger, and Jérôme Benveniste

***Abstract*—The backscatters power single-look waveform recorded by a synthetic aperture radar altimeter is approximated in a closed-form model. The model, being expressed in terms of parameterless functions, allows for efficient computation of the waveform and a clear understanding of how the various sea state and instrument parameters affect the waveform.**

***Index Terms*—Closed-form solutions, Earth observation systems, radar remote sensing, radar signal processing, sea level, sea surface, synthetic aperture radar.**

I. Introduction

A RADAR altimeter measures the distance between the instrument and a surface by recording the time delay between the emission of a pulse and the reception of its echo. Raney applied synthetic aperture radar (SAR) techniques to altimetry in an effort to improve measurement quality [1]. A review of SAR altimetry can be found in the literature [2].

The first test of a SAR altimeter was the NASA-funded Delay/Doppler Phase Monopulse (D2P) project [3] of The Johns Hopkins University Applied Physics Laboratory. The D2P instrument was an airborne SAR altimeter and interferometer and aimed to evaluate the efficacy of a SAR altimeter. At the same time, the European Space Agency (ESA) began to investigate the feasibility of a high-resolution satellite-based SAR altimeter, which led to the design and implementation of the Synthetic Interferometric Radar ALtimeter (SIRAL), the instrument currently flying onboard the Cryosat-2 satellite [4]. Cryosat-2 represents the first proof of concept of a satellite-based SAR altimeter, but its main objective is to monitor land and marine ice. Nevertheless, the capabilities of the new sensor for improved ocean observations have led to the selection by ESA of a SAR-based altimeter on board the forthcoming Sentinel-3 mission [5] of the European Global Monitoring for Environment and Security program, which will build on the strong heritage of the instrument techniques implemented for SIRAL on board Cryosat-2.

The extraction of ocean parameters from conventional altimetry waveforms relies on fitting the return echo with a theoretical model. The waveform model commonly used in classical radar altimetry was originally described in [7] and then in [6]. A closed-form analytical expression for the altimeter echo is provided (through some approximations) as the convolution of the average flat surface impulse response, the radar system point target response, and the probability density function of surface scattering elements [6], [7]. This model is the one adopted by the altimetry community to retrack the waveforms [8], and its closed-form formulation makes it perfectly suited for retracking a large number of echoes at an operational level.

Similarly to what has been developed for standard altimetry, studies have been carried out in recent years on the development of a theoretical model for SAR altimetry waveforms. These differ from the classical pulse-limited waveforms as a result of along-track processing and integration [9]. Their approach is very similar to that found in [6] and [7], in that the waveform is still modeled as a convolution of three different terms.

Some of the SAR altimeter response echo studies rely on a fully numerical calculation of the modeled waveforms [10], [11], whereas some others rely on a semianalytical model, where a closed-form expression is obtained for the three terms, and only the final convolution is numerically evaluated [12]–[14]. However, to date, no closed-form expression for the SAR altimeter return echo has been provided. As for conventional altimetry, a closed-form formulation is advantageous compared with numerical solutions, in that the amplitude and shape of the waveform can be directly linked to geophysical parameters, and a simple inversion procedure can be then used to retrieve these parameters. The aim of this paper is to provide a derivation of a compact closed-form model for the SAR altimetry return waveform from the ocean, along with some simulation results and comparison with real waveforms from Cryosat-2 data acquired over open ocean. This model has been developed within the framework of an ESA-funded project on the Development of SAR Altimetry Mode Studies and Applications over Ocean, Coastal Zones and Inland Water (SAMOSA).

II. Instrument Model

Here, we develop a mathematical model of the SAR altimeter and its backscattered waveform. The derivation of this model has been carried out specifically using parameters similar to those of the SIRAL instrument on board Cryosat. However, such derivation is here presented in a generalized form and should be applicable to a wide range of SAR altimeters.

Manuscript received October 18, 2013; revised February 15, 2014; accepted May 13, 2014.

C. Ray is with Saint Mary's College of California, Moraga, CA 94556 USA.

C. Martin-Puig is with isardSAT, 08042 Barcelona, Spain.

M. P. Clarizia is with the University of Michigan, Ann Arbor, MI 48109 USA.

G. Ruffini is with Starlab Barcelona SL, 08022 Barcelona, Spain.

S. Dinardo is with the European Space Research Institute (ESRIN), European Space Agency, 00044 Frascati, Italy, and also with Darmstadt Technical University, 64289 Darmstadt, Germany.

C. Gommenginger is with the National Oceanography Centre, Southampton SO14 3ZH, U.K.

J. Benveniste is with the European Space Research Institute (ESRIN), ESA, 00044 Frascati, Italy.

Digital Object Identifier 10.1109/TGRS.2014.2330423

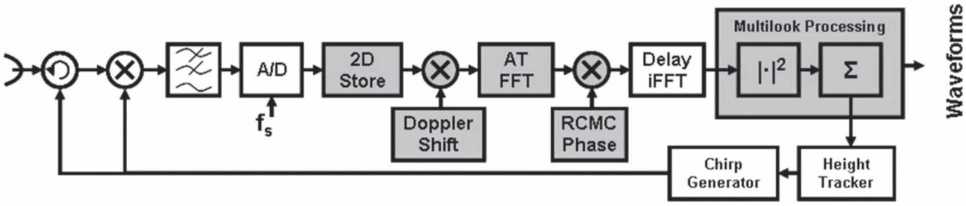

Fig. 1. Delay-Doppler altimetry block diagram.

A block diagram for a SAR altimeter is shown in Fig. 1 [1]. For a detailed explanation of the processing steps for SAR altimetry and its differences with respect to conventional altimetry, the reader is referred to [1] and [2].

The diagram has the following principle elements:

- generation and transmission of a burst of chirp pulses;
- reception of the echo from this burst and the multiplication of this signal by the complex conjugate of a delayed copy of the transmitted burst;
- discrete sampling of the product signal;
- Doppler correction;
- SAR processing [along-track fast Fourier transfrom (FFT)] to focus into beams in the along-track direction.
- range cell migration correction (RCMC);
- decoding of frequency encoded range [across-track inverse FFT (IFFT)].

In the sections to come, the model is developed following the steps of the block diagram.

A. Chirp Signal and Deramping

In order to allow SAR processing, a burst of N_b *chirp* pulses is transmitted from the altimeter. A single chirp pulse can be written as

$$\chi(t) = \begin{cases} e^{i2\pi(f_c t + \frac{1}{2}st^2)}, & \text{if } -\frac{\tau_p}{2} \leq t \leq \frac{\tau_p}{2} \\ 0, & \text{otherwise} \end{cases} \tag{1}$$

where f_c is the center frequency, s is the chirp slope, and τ_p is the chirp pulse duration. The bandwidth of the signal is $B_t = s\tau_p$. The transmitted burst of pulses can be written as

$$S_T(t) = \sum_{m=1-N_b/2}^{N_b/2} \chi(t - m/f_p + h/c) \tag{2}$$

where f_p is the pulse repetition frequency, N_b is the number of pulses in a burst, c is the speed of light, and h is the presumed distance between the instrument and the sea surface as estimated by the altimeter's onboard tracker. Note that $t = 0$ corresponds to the time when the center of the burst strikes the surface, not the time of transmission.

B. Range History of a Single Scatterer

Consider a single scatterer on the sea surface. From the rest frame of the satellite, the scatterer will be moving (along with the rest of the Earth's surface) so that the distance between the satellite and the scatterer $r(t)$ will change with time.

Using a right-hand coordinate system with an origin at the specular point on the sea surface and with z normal to the surface and x in the plane formed by the satellite velocity and z, we can write the range as

$$\begin{aligned} \frac{r(t)}{c} &\approx \frac{h}{c} + \frac{1}{2}\left[\frac{\alpha}{hc}(x^2+y^2) - \frac{2z}{c}\right] - \frac{1}{2}\left[\frac{2xv_t}{hc} - \frac{2v_r}{c}\right]t \\ &= \frac{h}{c} + \frac{1}{2}\tau_s - \frac{1}{2}\mu t \quad \text{with the obvious def} \end{aligned} \tag{3}$$

where $\alpha = 1 + (h/R)$, with R being the local radius of curvature of the Earth's surface; the initial location of the scatterer is (x, y, z); v_t and v_r are the tangential and radial velocities of the satellite as measured from an Earth-centered frame, respectively; and τ_s and μ are the collection of constants in the square brackets. In the preceding approximation, terms that contribute less than 4 ps have been dropped since this is small compared with the smallest scale in the system, the carrier period of 73 ps. It is worth noting that if we let x_s be the position of the Doppler zero relative to the specular point, then we can write $\mu = 2(x - x_s)v_t/(hc)$.

C. Reflected Signal

The signal at the scattering point is delayed by an amount $r(t)/c$, so that at a time t, the signal at the scattering point is

$$S_P(t) = S_T(t - r(t)/c). \tag{4}$$

This signal is then reflected back to the satellite and is thus delayed a further $r(t)/c$, so that the signal received at $t + r(t)/c$ is the same (apart from amplitude) as the signal at the point at time t, i.e.,

$$S_R(t + r(t)/c) = S_P(t) = S_T(t - r(t)/c). \tag{5}$$

Thus, we see we can write the received signal in terms of the transmitted

$$\begin{aligned} S_R(t + r(t)/c) &= S_T(t - r(t)/c) \\ S_R\left(t + \frac{h}{c} + \frac{\tau_s}{2} - \frac{\mu t}{2}\right) &= S_T\left(t - \frac{h}{c} - \frac{\tau_s}{2} + \frac{\mu t}{2}\right) \\ S_R\left(\left(1 - \frac{\mu}{2}\right)t + \frac{\tau_s}{2} + \frac{h}{c}\right) &= S_T\left(\left(1 + \frac{\mu}{2}\right)t - \frac{\tau_s}{2} - \frac{h}{c}\right) \\ S_R\left(t' + \frac{h}{c}\right) &= S_T\left(\frac{2+\mu}{2-\mu}t' - \frac{\tau_s}{1 - \frac{\mu}{2}} - \frac{h}{c}\right) \\ S_R\left(t' + \frac{h}{c}\right) &= S_T\left(t' - \frac{h}{c} - \tau_d\right) \end{aligned} \tag{6}$$

with $t' = (1 - \mu/2)t + (1/2)\tau_s$ and $\tau_d = \tau_s - \mu t'$. In the above, we have ignored terms that contribute less than 1 ps to the times since it is small compared with the carrier period of 74 ps.

D. Deramping

The first step after reception of the reflected signal is to multiply the signal with the complex conjugate of a copy of the transmitted signal delayed by $2h/c$. This is called deramping since it removes the frequency ramp of the chirp signal. The deramped signal is

$$D(t) = S_R(t + h/c)S_T^*(t - h/c). \tag{7}$$

The range of the scatterer is encoded as the frequency of the deramped signal. Using (6), we can write the deramped signal as

$$\begin{aligned} D(t) &= S_T(t - h/c - \tau_d)S_T^*(t - h/c) \\ &= \sum_{m=1-N_b/2}^{N_b/2} \chi(t - m/f_p - \tau_d)\chi^*(t - m/f_p). \end{aligned} \tag{8}$$

E. Discrete Sampling

Each burst is sampled by an analog-to-digital converter. Sample n of pulse m occurs at time $t_{n,m}$, with

$$t_{n,m} = \frac{m}{f_p} + \frac{n}{f_s} \tag{9}$$

where f_s is the sample rate; the index n is within the range with $1 - (N_p/2) \leq n \leq (N_p/2)$, and N_p is the number of samples per pulse. For future reference, we define the usable pulse length to be $\tau_u = N_p/f_s$. With $\tau_n = n/f_s$, we can write

$$\begin{aligned} D_{n,m} &= D(t_{n,m}) \\ &= \chi(\tau_n - \tau_d)\chi^*(\tau_n) \\ &= e^{i2\pi\left(f_c(\tau_n-\tau_d)+\frac{1}{2}s(\tau_n-\tau_d)^2\right)}e^{-i2\pi\left(f_c\tau_n+\frac{1}{2}s\tau_n^2\right)} \qquad (10) \\ &= e^{i2\pi\left(-f_c\tau_d-s\tau_n\tau_d+\frac{1}{2}s\tau_d^2\right)}. \qquad (11) \end{aligned}$$

By the definition of τ_d, we have $\tau_d = \tau_s - \mu t_{n,m}$. Putting this into the above and deleting terms that contribute less than a quarter of a cycle in phase, we arrive at

$$D_{n,m} \approx e^{i\phi_0}e^{-i2\pi s\tau_s n/f_s}e^{i2\pi f_c \mu m/f_p} \tag{12}$$

with $\phi_0 = 2\pi((1/2)s\tau_s^2 - f_c\tau_s)$. The multiplicative term $e^{i\phi_0}$ is a unit magnitude constant, independent of the indexes n and m and will be ignored from now on since it does not effect the power.

F. Doppler Correction

Because the satellite velocity is not perfectly tangent to the surface, the specular point does not naturally fall in the central Doppler bin. We can correct for this by multiplying the data matrix $D_{n,m}$ by a Doppler correction factor $e^{i2\pi f_c((2v_r)/c)(m/f_p)}$, i.e.,

$$\hat{D}_{n,m} = e^{i2\pi f_c \frac{2v_r}{c}\frac{m}{f_p}} \quad D_{n,m} = e^{-i2\pi s\tau_s \frac{n}{f_s}}e^{i2\pi\frac{x}{L_x}\frac{m}{N_b}} \tag{13}$$

with the definition

$$L_x = \frac{chf_p}{2v_t f_c N_b}. \tag{14}$$

G. Along-Track FFT

The next step in the signal processing chain is the SAR processing, which focuses the instrument in the along-track direction into N_b narrow beams. This is accomplished via a Fourier transform (FFT) across the different pulses of the burst. Sample n of beam ℓ is computed as follows:

$$\begin{aligned} \tilde{D}_{n,\ell} &= \sum_{m=1-N_b/2}^{N_b/2} w_m\hat{D}_{n,m}e^{-i2\pi\ell m/N_b} \\ &= e^{-i2\pi s\tau_s\frac{n}{f_s}}\sum_{m=1-N_b/2}^{N_b/2} w_m e^{i2\pi\left(\frac{x}{L_x}-\ell\right)m/N_b} \\ &= e^{-i2\pi s\tau_s\frac{n}{f_s}}N_b\Upsilon_{N_b}\left(\frac{x}{L_x} - \ell\right) \end{aligned} \tag{15}$$

where w_m is the windowing function employed in the FFT, and we define the function

$$\Upsilon_N(\xi) = \frac{1}{N}\sum_{m=1-N/2}^{N/2} w_m e^{i2\pi\xi m/N}. \tag{16}$$

In the case that $w_m = 1$, we have that

$$\Upsilon_N(\xi) = e^{i\pi\xi/N}\frac{\sin(\pi\xi)}{N\sin(\pi\xi/N)} \approx e^{i\pi\xi/N}\mathrm{sinc}(\xi). \tag{17}$$

In general, the function $\Upsilon_N(\xi)$ is strongly peaked at zero; thus, beam ℓ will be strongly peaked at the along-track position $x = L_x\ell$.

H. RCMC

The frequency of each beam ℓ needs to be offset in order for a particular range bin to correspond to the same across-track position for all beams. To this end, we multiply beam ℓ by the correction factor $e^{i2\pi s((\alpha L_x^2\ell^2 n)/(hcf_s))}$. The corrected beam is

$$C_{n,\ell} = e^{i2\pi s\frac{\alpha L_x^2\ell^2 n}{hcf_s}} \quad \tilde{D}_{n,\ell} = N_b\Upsilon_{N_b}(u)\, e^{-i2\pi k_\ell n/N_p} \tag{18}$$

with

$$u = \frac{x}{L_x} - \ell \tag{19}$$

$$k_\ell = \frac{L_x^2}{L_y^2}(u^2 + 2\ell u) + \frac{y^2}{L_y^2} - \frac{z}{L_z} \tag{20}$$

$$L_y = \sqrt{\frac{ch}{\alpha s\tau_u}} \quad L_z = \frac{c}{2s\tau_u}. \tag{21}$$

I. Across-Track IFFT

The final step in the processing chain is to compute the IFFT of each beam. This decodes the frequency encoded range.

Range k of beam ℓ is given by

$$\begin{aligned}\tilde{C}_{k,\ell} &= \frac{1}{N_p}\sum_{n=1-N_p/2}^{N_p/2} w_n C_{n,\ell} e^{i2\pi nk/N_p} \\ &= N_b \Upsilon_{N_b}(u)\Upsilon_{N_p}(k-k_\ell).\end{aligned} \tag{22}$$

The quantity $|\tilde{C}_{k,\ell}|^2$ gives the contribution by a point source at position (x,y,z) to the power in range bin k of beam ℓ. As a function of the scatterer position (x,y), the function $C_{k,\ell}$ is strongly peaked at the position $(x,y) = (L_x\ell, \pm L_y\sqrt{k+z/L_z})$, so that the power in cell (k,ℓ) is only due to scatterers near this position. In the case of $k < -z/L_z$, the peak occurs at $y = 0$.

J. Backscattered SAR Altimeter Power Waveform

Following Brown [7], we assume that the total backscattered power is the sum of the power of all the scatterers across the sea surface, as implied by the standard radar equation [16]. Thus, the total power in cell (k,ℓ) is given by

$$P_{k,\ell} = \int_{-\infty}^{\infty} dz\, p(z) \int_{-\infty}^{\infty} dx \int_{-\infty}^{\infty} dy \frac{\lambda_0^2 G^2(x,y)\sigma_0(x,y)}{4\pi r^4}|\tilde{C}_{k,\ell}|^2 \tag{23}$$

where $p(z)$ is the probability density distribution of the height of the point scatterers, G is the antenna power gain, and σ_0 is the normalized radar cross section.

K. Symmetrization

For notational convenience, we define the function Γ as the product of the gain and the radar cross section, i.e.,

$$\Gamma(x,y) = G^2(x,y)\sigma_0(x,y). \tag{24}$$

Using the definitions $\Gamma_e(x,y) = \Gamma(x,y) + \Gamma(x,-y)$ and $\Gamma_o(x,y) = \Gamma(x,y) - \Gamma(x,-y)$ can rewrite Γ as follows:

$$\Gamma(x,y) = \frac{1}{2}\Gamma_e(x,y) + \frac{1}{2}\Gamma_o(x,y). \tag{25}$$

The utility of this expression is that the first term Γ_e is an even function in y, whereas the second term Γ_o is odd. This is useful because, in computing the power $P_{k,\ell}$, the function Γ is integrated over y with $|\tilde{C}_{k,\ell}|^2/r^4$, which is itself even in y; thus, the odd part of Γ will integrate to zero, i.e.,

$$\begin{aligned}\int_{-\infty}^{\infty} dy\, \Gamma(x,y)\frac{|\tilde{C}_{k,\ell}|^2}{r^4} &= \int_{-\infty}^{\infty} dy \frac{1}{2}\Gamma_e(x,y)\frac{|\tilde{C}_{k,\ell}|^2}{r^4} \\ &= \int_{0}^{\infty} dy \Gamma_e(x,y)\frac{|\tilde{C}_{k,\ell}|^2}{r^4}.\end{aligned} \tag{26}$$

Thus, we can write the power as follows:

$$P_{k,\ell} = \int_{-\infty}^{\infty} dz\, p(z) \int_{-\infty}^{\infty} dx \int_{0}^{\infty} dy \frac{\lambda_0^2 \Gamma_e(x,y)}{4\pi r^4}|\tilde{C}_{k,\ell}|^2. \tag{27}$$

This has the computational advantage that $\tilde{C}_{k,\ell}$ has a single peak over this domain instead of the double peak over the full range of y.

L. Sea Height Model

We use the skewed Gaussian sea height probability density developed by Rodriguez [15], which can be written in the following form:

$$p(z) = \frac{1}{\sqrt{2\pi}\sigma_z}\left(1 + \frac{\lambda_s}{6}(\zeta^3 - 3\zeta)\right)e^{-\zeta^2/2}$$

with

$$\zeta = \frac{z - \langle z\rangle + z_{\mathrm{EM}}}{\sigma_z}. \tag{28}$$

The distribution is written in terms of the sea height mean $\langle z\rangle$, standard deviation σ_z, electromagnetic bias z_{EM}, and skewness λ_s. We assume the significant wave height to be $H_s = 4\sigma_z$.

III. Approximate Model

Here, we make approximations to the model waveform [see (23)] that will allow us to arrive to a closed-form expression of the waveform.

A. Slowly Varying Functions Approximation

Now, we recall that $\tilde{C}_{k,\ell}$ is sharply peaked around the point $(x,y) = (L_x\ell, L_y\sqrt{k+z/L_z})$, acting much like a 2-D δ-function in the x,y plane compared with the slowly varying functions Γ and $1/r^4$. Indeed, $1/r^4$ is very nearly a constant over the entire antenna footprint where $1/r^4 = 1/h^4$ within 0.04%. For this reason, we approximate

$$P_{k,\ell} \approx \frac{\lambda_0^2}{4\pi h^4}\int_{-\infty}^{\infty} dz\, p(z)\Gamma_{k,\ell}(z)\int_{-\infty}^{\infty} dx \int_{0}^{\infty} dy |\tilde{C}_{k,\ell}|^2 \tag{29}$$

with

$$\Gamma_{k,\ell}(z) = \begin{cases}\Gamma_e\left(L_x\ell, L_y\sqrt{k+z/L_z}\right), & \text{if } z > -L_z k \\ \Gamma_e(L_x\ell, 0), & \text{if } z < -L_z k.\end{cases} \tag{30}$$

Over the width of $|\tilde{C}_{k,\ell}|^2$, the function Γ_e varies by at most 2%, which we expect to lead to an error in the power significantly less than this because Γ_e is overestimated on one side of the center of $|\tilde{C}_{k,\ell}|^2$ and underestimated on the opposite side.

B. Linear Approximation of $\Gamma_{k,\ell}(z)$

A linear approximation to $\Gamma_{k,\ell}(z)$ can be made, i.e.,

$$\Gamma_{k,\ell}(z) \approx B_{k,\ell}(1 + T_{k,\ell}z/L_z) \tag{31}$$

with the following definitions:

$$B_{k,\ell} = \int_{-\infty}^{\infty} dz \frac{e^{-z^2/2\sigma^2}}{\sqrt{2\pi}\sigma}\Gamma_{k,\ell}(z) \tag{32}$$

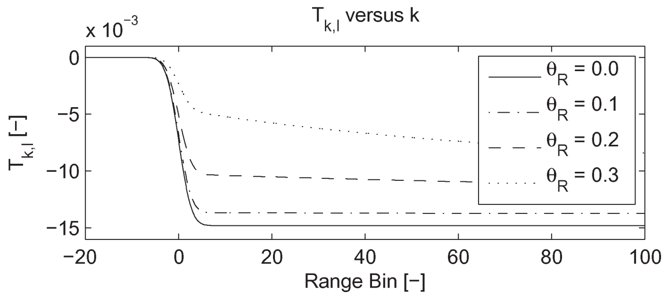

Fig. 2. Slope term of the linear approximation to Γ_e, for various significant wave heights (H_s) and roll mispointings (θ_R). Notice that $|T_{k,\ell}|$ is at most 0.015 and is thus a small parameter. In the case that the antenna gain can be approximated by a Gaussian, $T_{k,\ell}$ is independent of ℓ and is nearly independent of ℓ in any case.

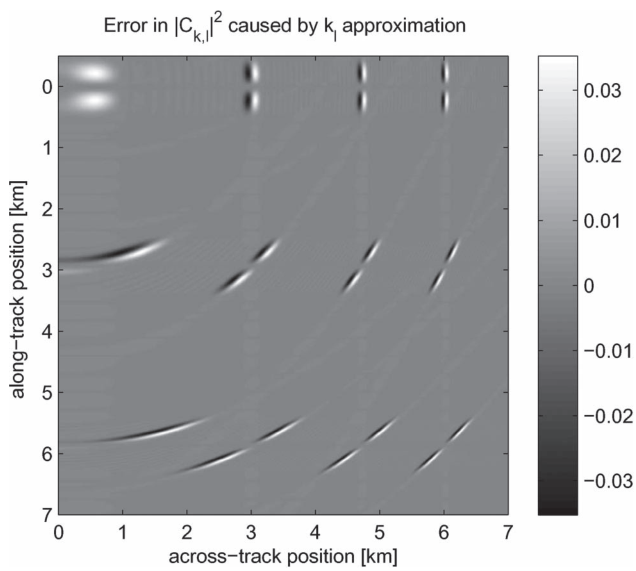

Fig. 3. Error caused in $|\tilde{C}_{k,\ell}|$ by the k_ℓ approximation. We can see that there is up to a $\pm 3\%$ error, but that the error is in a balanced way, except near $\ell = 0$, $k = 0$.

$$T_{k,\ell} = \frac{L_z}{B_{k,\ell}\sigma^2} \int_{-\infty}^{\infty} dz \frac{e^{-z^2/2\sigma^2}}{\sqrt{2\pi}\sigma} z\Gamma_{k,\ell}(z) \tag{33}$$

with $\sigma = 1.0$ m. The function $T_{k\ell}$ is computed and graphed in Fig. 2. We see that its magnitude is at most 0.015, indicating that the next order term will be even smaller and, thus, that the linear approximation is sufficient.

C. k_ℓ Approximation

Because $|\tilde{C}_{k,\ell}|$ is strongly peaked at $u = 0$, we know that u will be small over the nonzero region of integration. Thus, within the integral, we can expect the u^2 term to be small compared with u. For this reason, we are led to make the following approximation for k_ℓ [see (20)]:

$$k_\ell \approx \frac{L_x^2}{L_y^2} 2\ell u + \frac{y^2}{L_y^2} - \frac{z}{L_z}. \tag{34}$$

In Fig. 3, we see the error in $|\tilde{C}_{k,\ell}|$ caused by this approximation.

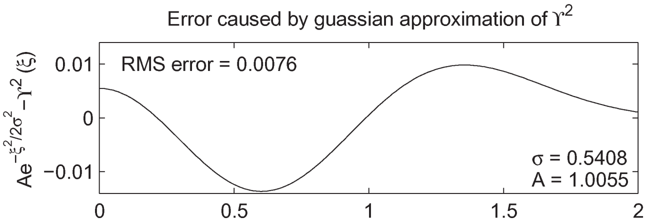

Fig. 4. Gaussian fit to Υ in the case of a hamming window.

D. Gaussian Approximation of Υ^2

We can approximate the function $\Upsilon(\xi)$ by a Gaussian, i.e.,

$$\Upsilon^2(\xi) \approx A_g e^{-\xi^2/2\sigma_g^2}. \tag{35}$$

In the case that a hamming window is used in the FFT, the Gaussian fit is quite good, with an RMS error of 0.76% over the region with the greatest error (see Fig. 4).

E. Final Expression

With the approximations listed above and discarding terms that have a coefficient $\lambda_s T_{k\ell}$, it is possible to arrive at the following form of the waveform:

$$P_{k,\ell} = K B_{k,\ell}\sqrt{g_l}\Bigg[(1 + T_{k,\ell}k_{\mathrm{off}})f_0(g_\ell\kappa) + T_{k,\ell}g_l\sigma_s^2 f_1(g_\ell\kappa) + \lambda_s \frac{g_l^3\sigma_s^3}{6}\left(3f_1(g_\ell\kappa) + f_3(g_\ell\kappa)\right)\Bigg] \tag{36}$$

with

$$K = \frac{\lambda_0^2 N_b^2 L_x L_y}{4\pi h^4}\sqrt{2\pi}A_g^2\sigma_g^2, \qquad \sigma_s = \frac{\sigma_z}{L_z} \tag{37}$$

$$k_{\mathrm{off}} = \frac{\langle z\rangle - z_{\mathrm{EM}}}{L_z} \qquad \kappa = k + k_{\mathrm{off}} \tag{38}$$

$$g_\ell = \left[\sigma_g^2 + \left(2\sigma_g \ell L_x^2/L_y^2\right)^2 + \sigma_s^2\right]^{-1/2} \tag{39}$$

$$f_n(\xi) = \int_0^\infty dv (v^2 - \xi)^n e^{-(v^2-\xi)^2/2}. \tag{40}$$

The combination $g_\ell\sigma_s < 1$ under all conditions; thus, we see that the third term has magnitude less than $\lambda_s/6$. Typical values of skewness are very small so that, in most cases, this term can be ignored, leading to

$$P_{k,\ell} = K B_{k,\ell}\sqrt{g_l}\left[(1 + T_{k,\ell}k_{\mathrm{off}})f_0(g_\ell\kappa) + T_{k,\ell}g_l\sigma_s^2 f_1(g_\ell\kappa)\right]. \tag{41}$$

If the onboard tracking is working correctly, then we expect $|k_{\mathrm{off}}| < 0.5$ so $|T_{k,\ell}k_{\mathrm{off}}| < 0.0075$. Thus, if a 1% error is acceptable, the waveform can be written as follows:

$$P_{k,\ell} = K B_{k,\ell}\sqrt{g_l}\left[f_0(g_\ell\kappa) + T_{k,\ell}g_l\sigma_s^2 f_1(g_\ell\kappa)\right]. \tag{42}$$

The last term has a coefficient $T_{k,\ell}g_l\sigma_s^2$, and $|T_{k,\ell}g_l\sigma_s^2| < 0.015\sigma_s = 0.015(H_s/(4L_z)) = (H_s/(125\ \mathrm{m}))$. Thus, we find that the f_1 term is only insignificant if the significant wave

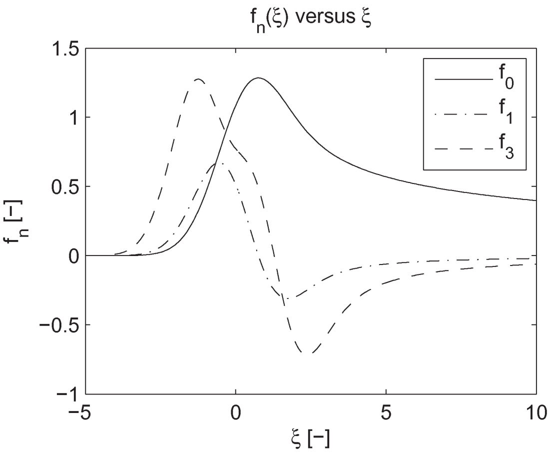

Fig. 5. Basis functions of the altimeter waveform.

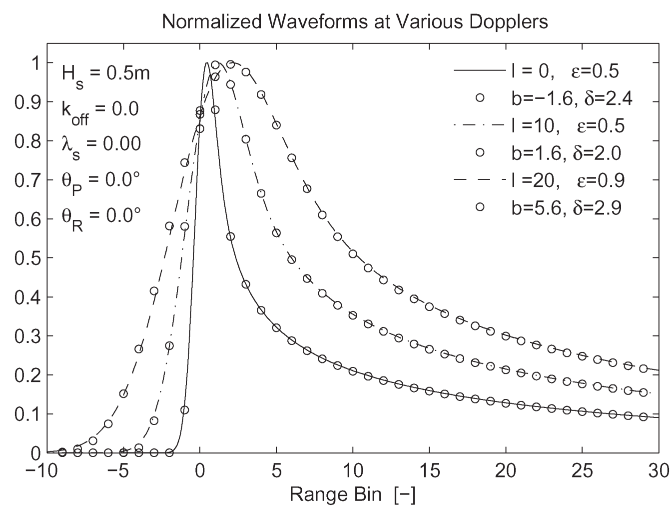

Fig. 6. Waveforms for a significant wave height of 0.5 m and for various Doppler beams ℓ. The solid line is the approximate model, and the circles are the full model.

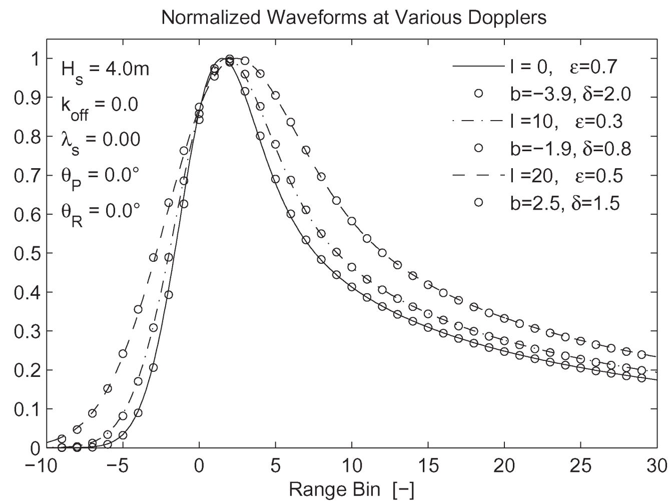

Fig. 7. Waveforms for a significant wave height of 4.0 m and for various Doppler beams ℓ. The solid line is the approximate model, and the circles are the full model.

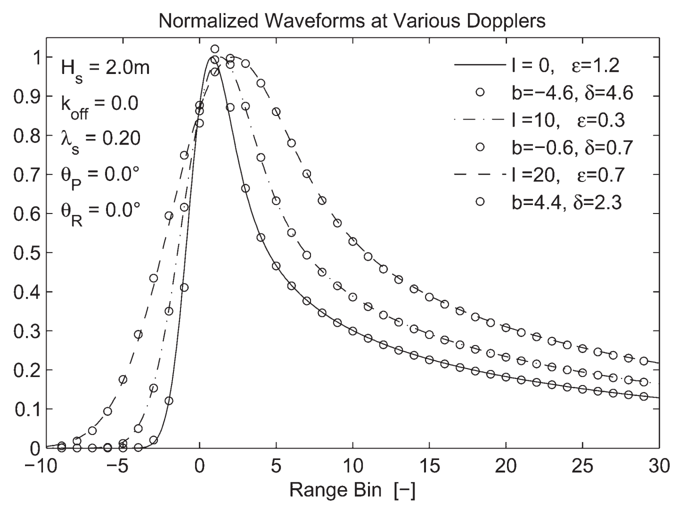

Fig. 8. Waveforms with skewness.

height is less than a meter or two, in which case the waveform is simply

$$P_{k,\ell} = KB_{k,\ell}\sqrt{g_l}f_0(g_\ell\kappa). \tag{43}$$

Notice that this implies that the waveforms in all of the beams are dilated version of the same function $f_0(g_\ell\kappa)$ with the only difference being the dilation rate g_ℓ. Having an analytical expression for this scaling factor g_ℓ should be useful in the analysis of the waveform.

In addition, notice that $B_{k,\ell}$ and $T_{k,\ell}$ depend only on the antenna gain, antenna pointing, and the backscatter cross section; whereas g_ℓ depends only on the configuration of the instrument and the significant wave height, and $f_n(\xi)$ does not depend on any parameters at all. Thus, the effects of the various influence on the waveform have been isolated in (36).

IV. Evaluation of Model

A. Comparison of the Approximate Model With the Full Model

Here, we evaluate the error caused by the approximations made in the previous section by comparing the waveforms produced by numerically integrating the full model [see (23)] with the waveform of the approximate model [see (36)]. In Figs. 6–11, both models are plotted for beams $\ell = 0, 10,$ and 20. The full model is plotted as circles, and the approximate model is plotted as a solid line. Both models have been plotted with the same amplitude scaling factor so that the amplitude of the approximate model is 1. Three measures of the difference are computed, i.e., the RMS difference ε, the maximum difference δ, and the range bias b. The values for ε and δ shown in the graphs have been multiplied by 100. The value of b is given in centimeters.

The figures plotted are typical. We can make the following general observations. The errors are remarkably constant over different parameters, indicating that the model accurately follows the changes caused by changing these parameters. The maximum error is less than 3%. The RMS error is less than 1% and typically less than 0.5%. The bias ranges from -1.5 cm for $\ell = 0$ to 5 cm for $\ell = 20$.

It was found that, with an improved but more complicated computation of $\Gamma_{k,\ell}(z)$, the bias at $\ell = 20$ was reduced to

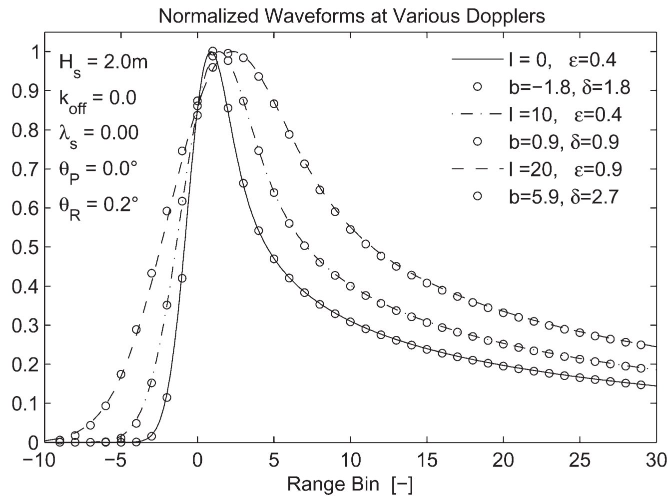

Fig. 9. Waveforms with mispointing in pitch.

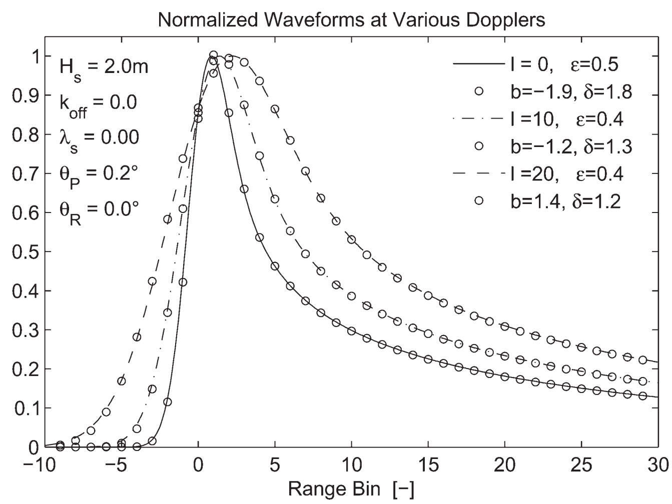

Fig. 10. Waveforms with mispointing in roll.

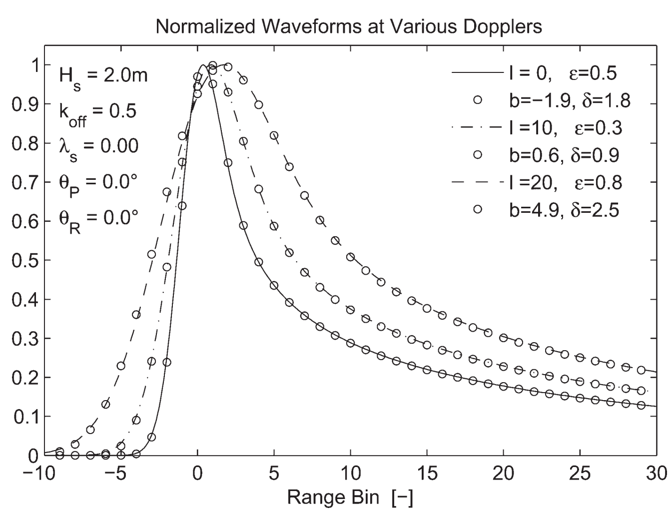

Fig. 11. Waveforms with a tracking point offset.

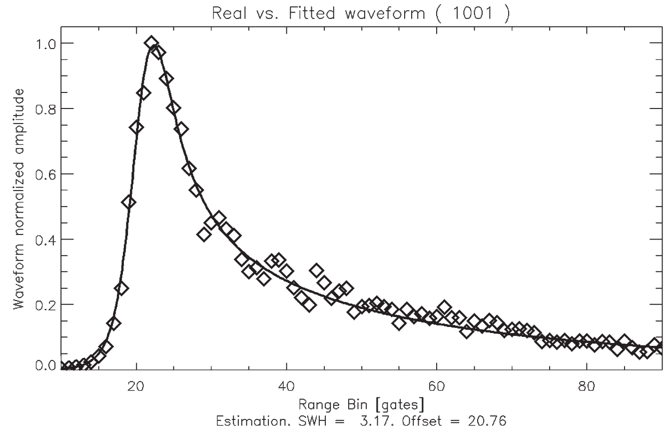

Fig. 12. Measured waveform from Cryosat-2 data, along with its best fit model waveform.

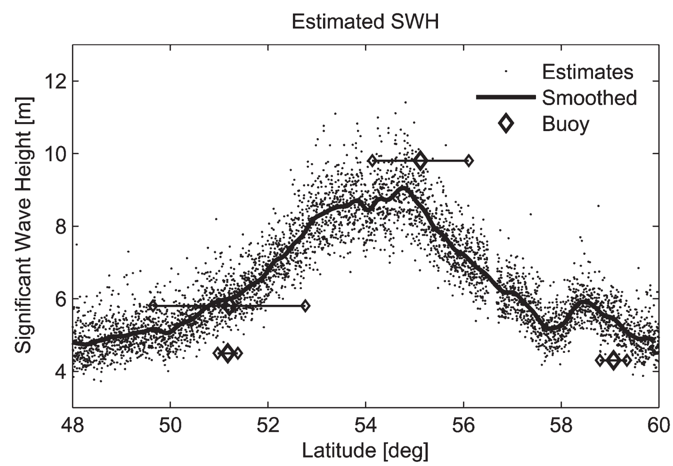

Fig. 13. Comparison of along-track SWH measurements as a function of latitude. The diamonds correspond to the SWH as measured by buoys; the bars indicated the distance of the buoy from the track. The small dots are the estimated SWH using the model waveform.

0.5 cm, but the bias at $\ell = 0$ was unaffected. In contrast, with a different k_ℓ approximation, the bias at $\ell = 0$ was removed. For this reason we, conclude that, for large ℓ, the Γ_e approximation is causing the error in the leading edge of the waveform that causes the bias, whereas for small ℓ, the bias is caused by the k_ℓ approximation.

V. Comparison With Cryosat Data

We provide now a preliminary comparison of the model with real data. A careful analysis of the usability of the model for waveform fitting has been performed by the others in the SAMOSA team and will be separately presented. The model waveform was used to retrack SAR altimeter waveforms from data collected by the Cryosat satellite on May 23, 2011, as it passed by the coast of Ireland. In Fig. 12, a typical best fit model multilook waveform is shown together with the measured waveform from Cryosat-2 data. The skewness was assumed to be zero for the fitting. The significant wave height (SWH) and $\langle z \rangle$ were estimated from the Cryosat-2 recorded waveforms. The SWH estimates have then been plotted in Fig. 13, along with plots of collocated buoy measurements. The distance between the buoys and the track has been represented as an uncertainty bar on the buoy location, although it is indeed a distance in longitude not latitude.

TABLE I
PARAMETERS OF THE SYSTEM AND SENSOR, TYPICAL OF THE SIRAL ALTIMETER ON BOARD CRYOSAT, USED TO PRODUCE THE SIMULATIONS

SYMBOL	DESCRIPTION	VALUE
f_c	Central frequency	13.575 GHz
τ_p	Pulse length	49 μs
τ_u	Usable pulse length	44.8 μs
s	Chirp slope	7.1438 MHz/μs
h	Nominal orbit height	717242 m
v_t	Nominal satellite velocity	7498 m/s
N_p	Number of samples per pulse	128
N_b	Number of pulses per burst	64
f_p	Pulse Repetition Frequency	17825 Hz
θ_x	Half-power along-track beam width	1.0766 Deg.
θ_y	Half-power across-track beam width	1.2016 Deg.

VI. CONCLUSION

A closed-form expression for the SAR altimeter waveform has been developed. The waveform is expressed in terms of a set of basis functions $f_n(\xi)$ that do not depend on any parameter of the system. The dependence of the waveform on the instrument and sea state parameters is clearly expressed. The most important result from this work is the observation that, to a good approximation, the waveforms in the different Doppler beams are dilated versions of the same waveform and that the scale of the dilation is set by the parameter g_ℓ.

PARAMETERS

The system parameters assumed in this paper are listed in Table I.

ACKNOWLEDGMENT

This work was made possible by the European Space Agency through the SAMOSA project. Author C. Ray would like to acknowledge the indispensable support of J. Marquez of Starlab and the support of Saint Mary's College of California through a faculty development grant and a sabbatical leave.

REFERENCES

[1] R. K. Raney, "The delay/Doppler radar altimeter," *IEEE Trans. Geosci. Remote Sens.*, vol. 36, no. 5, pp. 1578–1588, Sep. 1998.
[2] P. D. Cotton *et al.*, SAMOSA state of art assessment report, European Space Agency, Paris, USA. [Online]. Available: http://www.satoc.eu/projects/samosa/docs/SAMOSA-TN01-V1.0full.pdf
[3] R. K. Raney and J. R. Jensen, D2P Project: Test Campaign Results, Jun. 2000. [Online]. Available: http://fermi.jhuapl.edu/d2p
[4] J. R. Jensen and R. K. Raney, "CryoSat: A mission to determine the fluctuations in Earth's land and marine ice fields," *Adv. Space Res.*, vol. 37, no. 4, pp. 841–871, 2005.
[5] C. Donlon *et al.*, "The Global Monitoring for Environment and Security (GMES) Sentinel-3 mission," *Remote Sens. Environ.*, vol. 120, pp. 37–57, May 2012.
[6] G. S Hayne, "Radar altimeter mean return waveform from near-normal-incidence ocean surface scattering," *IEEE Trans. Antennas Propag.*, vol. AP-28, no. 5, pp. 687–692, Sep. 1980.
[7] G. S. Brown, "The average impulse response of a rough surface and its applications," *IEEE Trans. Antennas Propag.*, vol. AP-25, no. 1, pp. 67–74, Jan. 1977.
[8] L.-L. Fu and A. Cazenave, *Satellite Altimetry and Earth Science*. San Diego, CA, USA: Academic, 2001.
[9] L. Phalippou and V. Enjolras, "Re-tracking of SAR altimeter ocean power waveforms and related accuracies of sea surface height, significant wave height and wind speed," in *Proc. IEEE IGARSS*, 2007, pp. 3533–3536.
[10] L. Phalippou and F. Demeestere, "Accurate numerical forward model for optimal retracking of SIRAL2 SAR echoes over open ocean," presented at the American Geophysical Union, Fall Meeting, San Francisco, CA, USA, 2011, Paper C53F-05.
[11] F. Boy and T. Moreau, "Algorithm theoretical basis document for the CPP SAR numerical retracker for oceans," European Space Agency. [Online]. Available: http://www.satoc.eu/projects/CP40/docs/S3A-NT-SRAL-00099-CNES_SAR_ATBD.pdf
[12] K. Giles, D. Wingham, R. Cullen, N. Galin, and W. H. F. Smith, "Precise estimates of ocean surface parameters from CryoSat," in *Proc. OSTST Meet.*, Sep. 2012, pp. 1–13.
[13] A. Halimi *et al.*, "An analytical model for Doppler altimetry and its estimation algorithm," in *Proc. OSTST Meet.*, Sep. 2012, pp. 1–28.
[14] D. J. Wingham, L. Phalippou, C. Mavrocordatos, and D. Wallis, "The mean echo and echo cross-product from a beam forming, interferometric altimeter and their application to elevation measurement," *IEEE Trans. Geosci. Remote Sens.*, vol. 42, no. 10, pp. 2305–2323, Oct. 2004.
[15] E. Rodriguez, "Altimetry for non-Gaussian oceans: Height biases and estimation of parameters," *J. Geophys. Res.*, vol. 93, no. C11, pp. 14 107–14 120, Nov. 1988.
[16] F. T. Ulaby, R. Moore, and A. Fung, "Microwave remote sensing, active and passive," in *VOL. II: Radar Remote Sensing and Surface Scattering and Emission Theory*. Reading, MA, USA: Addison-Wesley, 1982.

Chris Ray received the Ph.D. degree in physics from the University of California, Davis, CA, USA, in 1994.

He is currently a Professor of physics with Saint Mary's College of California, Moraga, CA, USA. Since 2001, he has been collaborating with Starlab.

Cristina Martin-Puig received the B.Sc. degree in electrical engineering from the Escola Técnica Superior d'Enginyeria de Telecomunicació de Barcelona (BCN), Barcelona, Spain, in 2003 and the M.Sc. degree in electrical engineering from Stanford University, Stanford, CA, USA, in 2004.

In 2002, she joined the Radar Interferometry Group at Stanford University as a Visiting Researcher to undertake her B.Sc. thesis. Since 2006, she has been involved in a wide variety of contracts with the European Space Agency, Paris, France, in synthetic aperture radar altimetry.

Maria Paola Clarizia (S'08–M'14) received the M.S. (*summa cum laude*) degree in telecommunications engineering in 2007 from the University of Sannio, Benevento, Italy, and the Ph.D. degree in Global Navigation Satellite System (GNSS) reflectometry from the University of Southampton, Southampton, U.K., in 2012.

She has worked as a Research Engineer in the field of SAR altimetry and GNSS reflectometry for Starlab Barcelona SL and as a Research Scientist in the field of GNSS reflectometry for the Natural Environment Research Council at the National Oceanography Centre in Southampton. In April 2013, she joined the University of Michigan, Ann Arbor, MI, USA, as a Postdoctoral Research Fellow, working on calibration and wind speed retrieval algorithms for the NASA Cyclone Global Navigation Satellite System (CYGNSS) mission. Her research interests are in GNSS reflectometry, altimetry (conventional, SAR, coastal), GNSS radio occultation, sea surface simulations and electromagnetic scattering models, data analysis, and statistical processing.

Giulio Ruffini was born in Barcelona, Spain, 1966. He received the Bachelor's degree in mathematics and physics from the University of California, Berkeley, CA, USA, and the Ph.D. degree in physics from the University of California, Davis, CA, in 1995.

He is the Chief Executive Officer of Starlab Barcelona SL, Barcelona. He has led several European Space Agency and European Union projects on technology development in Earth observation and biomedical applications.

Salvatore Dinardo received the M.Sc. (with first-class honors) degree in aerospace engineering from Seconda Universitá degli Studi di Napoli, Caserta, Italy. He is currently working toward the Ph.D. degree at Darmstadt Technical University, Darmstadt, Germany.

Since 2008, he has been a Serco Contractor on site with ESA/ESRIN, providing support and expertise in radar altimetry in the ESA Earth Observation Science, Applications and Future Technologies Department. He has been involved in several ESA exploitation projects for the past and flying radar altimetry missions, as well as in the preparation of following radar altimetry missions.

Christine Gommenginger received the Ph.D. degree from Southampton University, Southampton, U.K., on the application of low grazing angle marine radar images for dynamic ocean feature monitoring.

She is currently a Senior Research Fellow with the National Oceanography Centre, Southampton, U.K. She has wide-ranging interests in the exploitation of ocean remote sensing data for oceanographic and applied research and operational applications. As a physical oceanographer by training, her work focuses on developing new and improved measurements of wind, waves, sea level, salinity, and currents using a range of microwave remote sensing techniques.

Jérôme Benveniste received the Ph.D. degree from University Paul Sabatier in Toulouse, France, in 1989.

After receiving the Ph.D. degree in oceanography from space, and a postdoctoral fellowship with the Massachusetts Institute of Technology, Boston, MA, USA, in space data assimilation in ocean models, he has been with the European Space Agency since 1992, at the Earth Observation data center near Rome, Italy, where he is in charge of the ERS-1, ERS-2, and ENVISAT radar altimeter data exploitation, interaction with ESA EO principal investigators, organizing scientific symposia, and launching research and development (R&D) projects, including CryoSat and GOCE data exploitation and preparing for the scientific exploitation of the Sentinel-3 Radar Altimetry. He initiated the SAMOSA R&D activity in 2007. He is a Coeditor of a Springer book on Coastal Zone Radar Altimetry published in 2011 and one on Inland Water Altimetry to be published in 2015.

Dr. Benveniste was elected Chair of COSPAR Oceanography Commission in 2008 and was reelected in 2012. He coorganized the OceanObs'09 Conference and the 15 and 20 Years of Progress in Radar Altimetry Symposium (2006 and 2012).